Small

www.small-journal.com

RESEARCH ARTICLE

Cuttlefish Ink-Derived Melanin/MXene Composites: Boosting Stability and Unleashing Synergistic Photothermal-Mechanical Antimicrobial Effects Against Biofilms

Zhenxing Tan[1] | Xiaotong Huang[1] | Dandan Zhang[1] | Hao Huang[1] | Rongrong Hu[1] | Caijie Ding[1] | Wenxia Wang[1] | Yong Yuan[2] | Lihua Zhou[1]

[1]School of biomedical and pharmaceutical sciences, Guangdong University of Technology, Guangzhou, P. R. China | [2]Guangdong Key Laboratory of Environmental Catalysis and Health Risk Control, School of Environmental Science and Engineering, Institute of Environmental Health and Pollution Control, Guangdong University of Technology, Guangzhou, P. R. China

Correspondence: Lihua Zhou (qhzhoulh@gdut.edu.cn)

Received: 5 January 2026 | **Revised:** 1 May 2026 | **Accepted:** 13 May 2026

Keywords: antimicrobial nanomaterials | MXene | natural melanin | oxidative stability | photothermal-mechanical synergistic effect

ABSTRACT

The advancement of MXene-based antibacterial platforms has been impeded by two critical limitations. Specifically, these include rapid oxidative degradation in physiological environments and potential cytotoxicity derived from their metallic nature. To address these challenges, we develop a core-shell structured nanikohybrid (CI@MXene) through the integration of natural cuttlefish ink melanin (CI) with MXene nanosheets. This biomimetic design establishes a protective barrier that effectively prevents MXene oxidation, thereby preserving its structural integrity and granting it durable antibacterial activity with sustained efficacy even after prolonged storage. Furthermore, the composite enables a mild photothermal therapy (PTT) under near-infrared irradiation, maintaining skin temperature below 45°C. This gentle thermal effect synergizes with the preserved nano-knife capability of the encapsulated MXene, resulting in remarkable eradication rates exceeding 95% against both *E. coil* and *S. aureus*, along with approximately 80% disruption of established biofilms. More importantly, in vivo evaluation using a murine wound infection model demonstrated accelerated wound closure, significantly reduced bacterial burden, and attenuated inflammatory responses, accompanied by enhanced tissue regeneration. This work not only provides fundamental insights into the rational design of stable and biosafe MXene-based nanomaterials but also establishes a novel strategy for synergistic physical antibacterial therapy, offering a promising approach for combating biofilm-associated infections.

1 | Introduction

The skin, acting as the primary barrier against external infections, is susceptible to infection by pathogenic bacteria in cases of open wounds, burn wounds, postoperative incisions, and other types of wounds. This not only hinders wound healing and complicated treatment, but also can result in severe complications, including systemic infections [1–3]. While escalating antibiotic doses is a conventional strategy against bacterial and biofilm infections, it unintentionally exacerbates the critical public health threat of antibiotic resistance [4, 5]. Consequently, there is an urgent need to develop safe, efficient, broad-spectrum and non-resistant antimicrobial materials to replace the use of traditional antibiotics.

Small, 2026; 0:e73934
https://doi.org/10.1002/smll.73934

Two-dimensional MXene nanosheets, characterized by excellent photothermal and mechanical properties due to their large surface area, ultrathin structure, and abundant free-electron distribution, have recently emerged as promising photothermal therapy (PTT) antibacterial agents [6–8]. However, a crucial limitation of MXene is its susceptibility to oxidative degradation in physiological environments, which diminishes its photothermal stability and leads to uncontrolled temperature increases. This poses a potential risk to healthy tissues and may impede the healing process [9–12]. Furthermore, oxidized MXene tends to agglomerate, compromising its dispersion stability in vivo, while the biocompatibility of high-dose MXene requires further improvement [13]. Numerous studies have proposed strategies to enhance MXene's stability. For instance, Lin et al. combined MXene with soybean phospholipids (SPs) to reduce its zeta potential and enhance colloidal stability [14]. Similarly, Liu et al. coated MXene nanosheets with polydopamine (PDA) to prevent oxidation and improve antimicrobial efficacy [15]. Nevertheless, prevailing strategies often fail to fully prevent oxidative degradation during use or rely on costly stabilizers and complex procedures.

Cuttlefish ink melanin (CI), a natural pigment derived from melanin-rich waste of cuttlefish ink sacs, can be extracted readily via centrifugation [16]. Despite its availability, CI is disregarded frequently instead of being employed as a functional material. In fact, CI possesses inherent broad-spectrum light absorption characteristic of melanins. Additionally, the metal-binding surface sites, (such as —COOH, —OH, etc.), enable CI to have stable chelating capacities toward metal ions. These properties make it a promising candidate for applications in photothermal therapy or as a surface-modifying agent [17]. For instance, Xue et al. combined CI with hydrophobic SiO_2 to develop an anti-icing coating capable of self-deicing [18]. Chemically, CI is a polymeric material consisting mainly of 5,6-dihydroxyindole (DHI) and 5,6-dihydroxyindole-2-carboxylic acid (DHICA). Its abundant catechol groups contribute not only to antibacterial activity but also to high antioxidant capacity and biocompatibility, which have led to growing interest in its biomedical applications in recent years [19–22]. Further expanding its utility, Zhang et al. incorporated CI with mitochondria-targeting functional units and SiO_2 to construct yolk–shell nanostructures for NIR-II photothermal combination cancer therapy [23]. Similarly, Jiang et al. developed red blood cell (RBC) membrane-coated CI nanoparticles (Melanin@RBC) as an in vivo photothermal anti-tumor platform, which improved tumor-specific accumulation and exhibited good biodegradability [24].

Based on the above considerations, this study utilized CI as a modifier, which uniformly coated the hydrophilic surface of MXene via hydrogen bonding, thereby effectively retarding its oxidation and forming a stable CI@MXene composite. CI act as sacrificial antioxidants to preferentially scavenge dissolved oxygen and reactive oxygen species in the environment, thereby effectively protecting the fragile Ti-C inorganic framework of MXene from oxidative attack. Meanwhile, the CI coating on the surface of the MXene nanosheets forms a physical barrier that reduces direct contact between MXene and oxidizing agents, further helping to inhibit oxidation. The composite retains favorable mechanical properties and demonstrates outstanding photothermal conversion efficiency, enabling a robust response to NIR light and conferring broad-spectrum antibacterial and biofilm ablation capabilities via a synergistic "mechanical-thermal effect" [25–27]. Furthermore, the incorporation of CI significantly enhances the biocompatibility of the composite. In vivo experiments established that CI@MXene effectively alleviates inflammatory symptoms induced by bacterial infection and promotes wound healing. Thus, the CI-modified MXene composite exhibits comprehensive performance advantages in terms of stability, mechanical properties, photothermal performance, and biocompatibility, highlighting its strong potential for broader biomedical applications (Scheme 1).

2 | Results and Discussion

2.1 | Characterization of the Materials

Observed in Figure 1a,d, MXene displays a near-transparent, flake-like morphology with a layer number ranging from single to few layers and lateral dimensions of approximately 0.5–2.0 µm. Magnified views reveal regions where multiple MXene nanosheets are stacked, consistent with its dark green aqueous dispersion. In contrast, the CI aqueous dispersion is brown in color. TEM images of dried and ground CI powder show near-spherical particles with sizes between 100 and 250 nm (Figure 1b,e). The CI@MXene composite was prepared via a straightforward mechanical stirring complexation process. HAADF-STEM images (Figure 1c,f) reveal a "core-shell-like" architecture within the composite, where CI nanospheres are encapsulated by MXene nanosheets. The surface of the CI nanospheres was coated with crumpled edges of MXene, resulting in a rough surface morphology. EDX elemental mapping (Figure 1g) was used to further characterize the interface of the CI@MXene composite. The C and Ti elemental signals exhibit nearly complete overlap with the CI nanospheres and MXene nanosheets, respectively. Owing to the abundance of surface oxygen-containing functional groups on both CI and MXene, oxygen was distributed across both components. Most notably, the correspondence between C and Ti elements clearly confirms that MXene nanosheets are layered over the surface of the CI nanospheres.

In the FTIR spectra of Figure 2a, CI, a melanin rich in DHI and DHICA, exhibits a sharp peak at 1630 cm^{-1} and a weak, broad absorption band between 600–-800 cm^{-1}, which can be attributed to its aromatic conjugated system. A strong, broad peak at 3400 cm^{-1} corresponds to abundant surface hydrophilic groups (e.g., —OH, —NH_2) [28]. MXene shows a broad and intense characteristic peak at 546 cm^{-1}, indicative of abundant surface terminal —OH groups [29]. After incorporation of CI, the FTIR spectrum of the CI@MXene composite retains the characteristic absorption bands of CI at 3400 and 1630 cm^{-1}, as well as the MXene-derived peak at 546 cm^{-1}. Notably, the intensity of the MXene terminal —OH peak at 546 cm^{-1} was significantly reduced, suggesting that most of these groups were grafted onto CI via hydrogen bonding. These results confirm the successful preparation of CI@MXene composites through a simple stirring process, with uniform grafting of CI onto thin MXene nanosheets while maintaining excellent hydrophilicity.

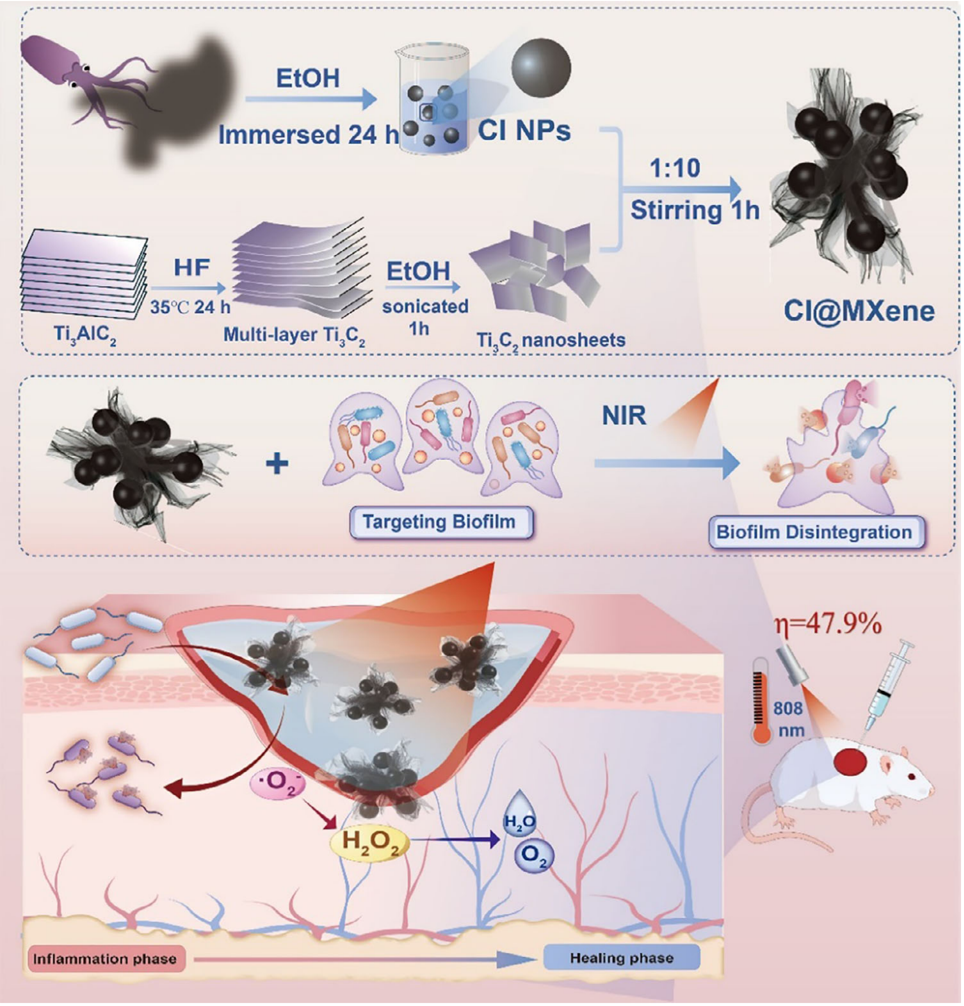

SCHEME 1 | Schematic illustration of CI@MXene-mediated antibacterial mechanisms and promotion of infected wound healing.

XRD was conducted to analyze the crystalline structures of the materials (Figure 2b). CI displayed a broad peak near 25°, corresponding to the (002) plane of graphite, suggesting that it is primarily amorphous with partial graphitization. The ultrasonically exfoliated MXene nanosheets showed a strong (002) peak at $2\theta \approx 6.9°$, consistent with reported values for thin-layer MXene [30]. Additional peaks observed at $2\theta \approx 18°$ and 27° are assignable to $Ti_3C_2(OH)_2$, confirming the presence of surface -OH groups [31]. In the XRD pattern of CI@MXene, the characteristic (002) peak of MXene shifted slightly to a lower angle ($2\theta \approx 6.5°$), likely due to the insertion of CI nanoparticles expanding the interlayer spacing. Moreover, possibly due to the relatively low content and amorphous nature of CI, no distinct diffraction peaks corresponding to CI were detected in the CI@MXene composite.

The survey XPS spectra of MXene confirm the presence of C, O, Ti, and F, while the CI@MXene composite additionally exhibits a nitrogen signal originating from CI. Compared to MXene, the CI@MXene composite shows significantly increased atomic percentages of carbon and oxygen, along with a slight decrease in titanium content (Figure 2c). High-resolution spectra of each element were analyzed subsequently. As shown in the C 1s spectrum (Figure 2d), both the CI@MXene composite and MXene could be deconvoluted into characteristic bonds including C—Ti, C—Ti—O, C—C, C—O, and O—C═O [32]. Additionally, the C 1s spectrum of CI@MXene exhibited a component assignable to C-N, derived from CI, further confirming the successful anchoring of CI onto MXene. The O 1s fine spectrum (Figure 2e) was deconvoluted into contributions from Ti—O, TiO_2, C—Ti—O, and C═O species. Notably, the atomic percentage of Ti—O increased significantly from 10.1% in MXene to 27.0% in the CI@MXene composite, providing strong evidence of crosslinking between CI nanospheres and MXene nanosheets. Changes in the intensities of the TiO_2 and C—Ti—O peaks further indicate that CI occupies surface hydroxyl groups during grafting, consistent with interaction through hydrogen bonding. These observations align well with the FTIR results. The high-resolution Ti 2p spectra (Figure 2f) of both materials were fitted with doublets corresponding to Ti—C $2p_{3/2}$, Ti^{2+}/Ti^{3+} $2p_{3/2}$, Ti—O $2p_{3/2}$, Ti-C $2p_{1/2}$, Ti^{2+}/Ti^{3+} $2p_{1/2}$, and Ti—O $2p_{1/2}$, located at binding energies of 454.9, 456.2, 459.2, 461.0, 462.3, and 464.9 eV, respectively. Importantly, the Ti—O $2p_{3/2}$ peak showed no pronounced enhancement in the CI@MXene composite compared to MXene, with atomic percentages of 33.1% and 28.5%, respectively, suggesting that the composite structure mitigates MXene oxidation.

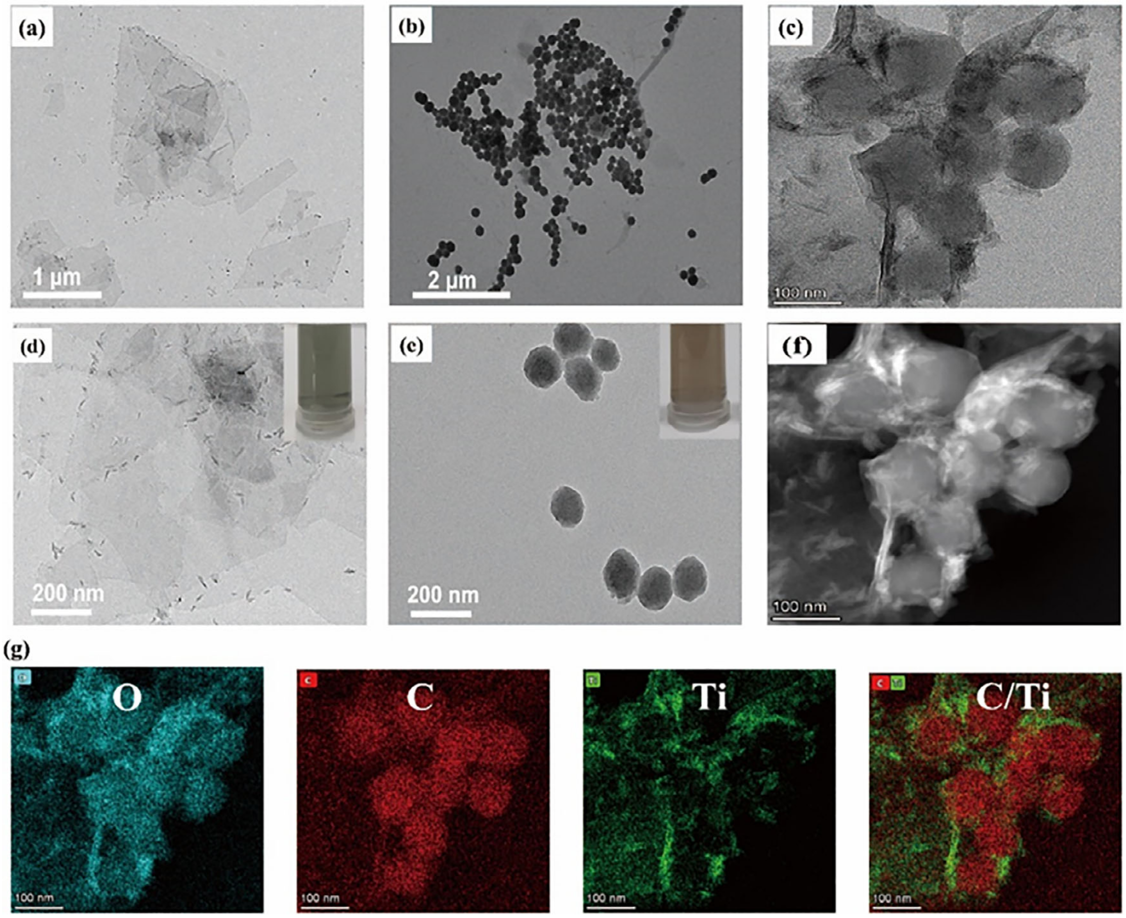

FIGURE 1 | (a,d) TEM images of MXene. (b,e) TEM images of CI. (c,f,g) HAADF-STEM and EDX elemental mapping of CI@MXene.

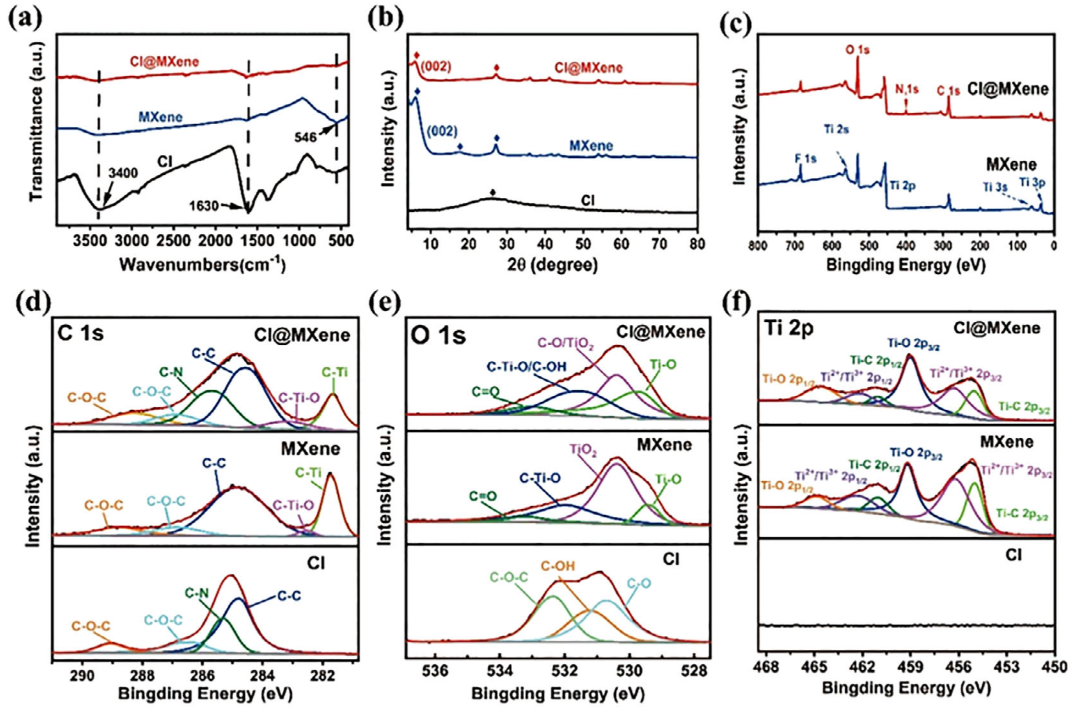

FIGURE 2 | Structural and compositional characterization of MXene, CI, and CI@MXene. (a) FTIR spectra, (b) XRD patterns, (c) XPS survey spectra, and high-resolution XPS spectra of (d) C 1s, (e) O 1s, and (f) Ti 2p.

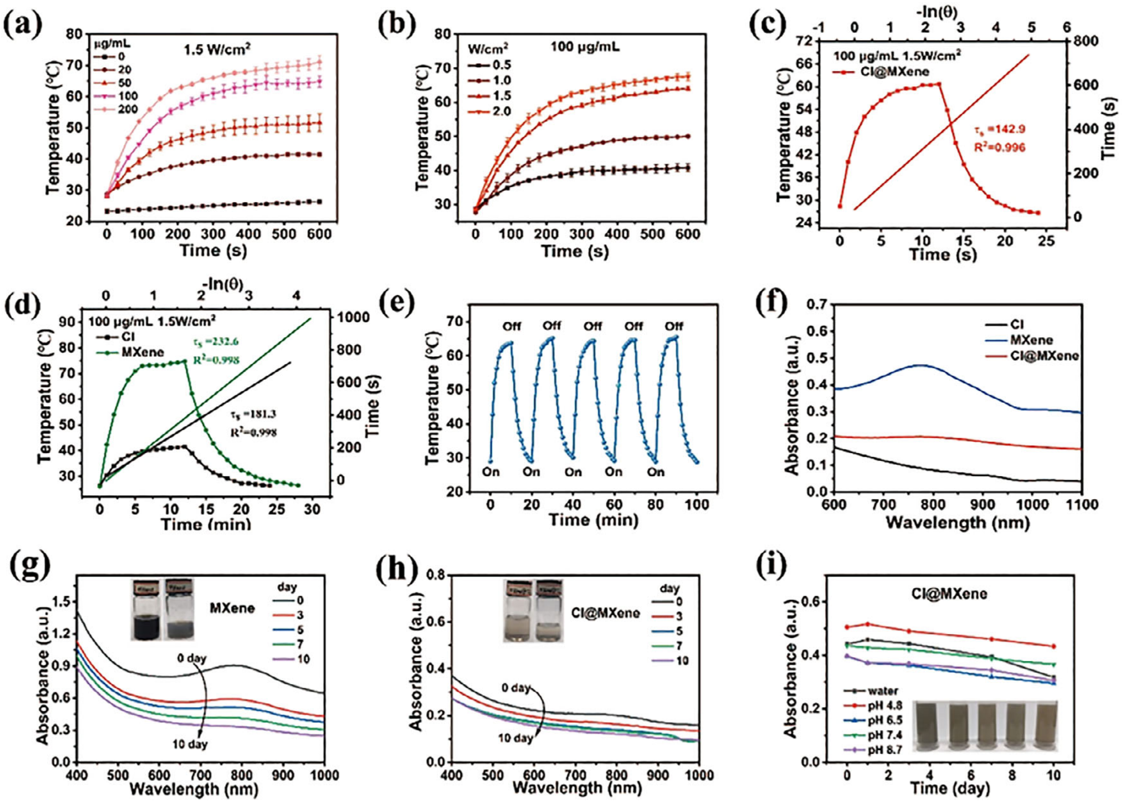

FIGURE 3 | Warming curves of CI@MXene composites at different concentrations (a) and different laser power densities (b) by 808 nm laser irradiation. (c) and (d) the linear fits of heating-cooling curves and the negative natural logarithm of CI@MXene, CI and MXene, respectively. (e) five cycles of CI@MXene. (f) absorption spectra of MXene, CI and CI@MXene (150 μg/mL). (g) UV absorption change of MXene and (h) CI@MXene left at room temperature. (i) 808 nm absorbance change of CI@MXene composites at different pH. Data are presented as mean ± SD ($n = 3$).

2.2 | Evaluation the Photothermal Efficiency and Stability of CI@MXene

The effect of different MXene-to-CI mass ratios on the photothermal performance of CI@MXene was evaluated. As illustrated in Table S1 and Figure S1, composites with elevated MXene content exhibited significantly higher temperature increments compared to CI-dominated counterparts. This enhancement can be attributed to the superior intrinsic photothermal conversion efficiency of MXene. The photothermal performance markedly improved with increasing MXene content and reached an optimum at a mass ratio of 10:1 (MXene:CI), yielding a temperature rise of 36.5°C within 10 min-nearly comparable to that of MXene. Although the maximum temperature difference was achieved at a 20:1 ratio, TEM images (Figure S1) revealed significant stacking of MXene nanosheets and sparse distribution of CI at this higher ratio, which reduced the availability of monolayer nanosheets and limited photothermal efficiency. Therefore, a 10:1 ratio yielded the optimal performance, enabling CI@MXene to deliver superior photothermal antibacterial performance.

The photothermal performance of the optimally loaded CI@MXene composite was evaluated by measuring its temperature rise profiles under varying concentrations and laser power densities (Figure 3a,b). At 100 μg/mL, the temperature of the CI@MXene dispersion increased by approximately 40°C above ambient temperature-sufficient for effective photothermal antibacterial treatment [33]. The temperature increase exhibited a concentration-dependent manner, and a heating trend comparable to that at 2.0 W/cm^2 was observed even at the lower power density of 1.5 W/cm^2. The heating and cooling behaviors of different materials were further compared (Figure 3c,d). Based on calculations, the η of CI@MXene reached 42.1%, significantly higher than that of CI (34.9%) and approaching that of MXene (47.9%). Moreover, this performance surpassed several commonly reported photothermal agents, including gold nanorods (21.0%) [34], CuS nanoparticles (16.3%) [35], and MoS$_2$ nanosheets (25.68%) [36]. Excellent photostability was confirmed through five on/off NIR cycles (Figure 3e), with no significant decay in the maximum temperature, underscoring the composite's suitability for repeated photothermal applications. As illustrated in Figure 3f, the NIR absorption spectra of MXene, CI, and CI@MXene composites were characterized using UV–vis spectrophotometry. Despite the superior absorbance of MXene at 808 nm, the CI@MXene composite achieved the better photothermal conversion efficiency. This apparent difference indicated that efficient photothermal performance depends not only on light absorption but more critically on the rate of hot electron generation [37]. The integration of CI accelerated the relaxation process of hot electrons, allowing their energy converted into lattice heat effectively, thereby enhancing photothermal conversion efficiency [38].

As the UV–vis spectra shown in Figure 3g,h, after being stored at room temperature for 10 days, the absorbance of the MXene aqueous solution decreased markedly over time, while that of the CI@MXene composite decreased only slightly. The inset photographs reveal that the MXene solution exhibited visible oxidation-induced color change, whereas the CI@MXene solution remained largely unchanged, further confirming the significantly enhanced stability of the composite. As shown the TEM images exhibited in Figure S2, after 40 days of storage, pronounced oxidation is observed in the MXene material: TiO_2 nanoparticles generated from oxidation expanded from the edges toward the center of the nanosheets and eventually aggregated across the surface (Figure S2a,d) [39]. In contrast, CI@MXene largely retained its original morphology even after the same period (Figure S2b,e). A magnified view of the edge region showed no significant signs of oxidation (Figure S2c,f), suggesting that CI was uniformly loaded and effectively shielded the MXene nanosheets. Furthermore, the stability of CI@MXene was evaluated in aqueous solutions of different pH values. No substantial decrease in stability was observed in either water or PBS buffer across a range of pH conditions. The composite maintained high structural integrity in both acidic and alkaline environments (Figure 3i), underscoring its suitability for applications under diverse physiological and chemical conditions.

To quantitatively evaluate the long-term oxidation stability of CI@MXene, we performed XPS analysis of Ti 2p core-level spectra after 0 day, 1 and 3 month of storage at room temperature (Figure S3). The relative contents of different Ti oxidation states were calculated from the peak areas and summarized in Tables S2 and S3. For MXene, the relative content of low-valence Ti (Ti^{2+}/Ti^{3+}), which represents the intact Ti—C inorganic skeleton, decreased sharply from 57.61% at day 0 to 32.82% after 3 months of storage, accompanied by a significant increase in TiO_2 content from 20.38% to 34.51%. This change in oxidation states indicates severe oxidative degradation of the MXene nanosheets, consistent with the observed color fading and photothermal performance attenuation. In sharp contrast, CI@MXene maintained a much higher Ti^{2+}/Ti^{3+} content of 46.74% and a lower TiO_2 content of 21.17% after the same 3-month storage period. Notably, the decrease in low-valence Ti content for CI@MXene was only 8.39%, which is less than one-third of the 24.79% decrease observed for MXene. These quantitative XPS results provide direct and rigorous evidence that CI modification significantly enhances the oxidation resistance of MXene nanosheets.

2.3 | In Vitro Antibacterial Activity of CI@MXene

The antibacterial efficacy of CI@MXene was systematically evaluated in vitro using the plate count method against *E. coli* and *S. aureus*. As shown in Figure S4, the antibacterial effect of CI@MXene was concentration-dependent. In the absence of NIR irradiation, increasing concentrations of CI@MXene resulted in a moderate reduction in bacterial survival, which may be attributed to mechanical disruption by MXene nanosheets and the presence of catechol groups in CI [40]. In contrast, under NIR irradiation, bacterial survival decreased significantly. Nearly complete bacterial eradication was observed at CI@MXene concentrations of 100–-120 µg/mL for *E. coli* and 120–-150 µg/mL for *S. aureus*. At a concentration of 200 µg/mL, no viable bacteria were detected, indicating total elimination of both bacterial strains. Based on a comprehensive assessment of antimicrobial efficacy, biosafety, and in vivo photothermal safety, we selected 120 µg/mL as the concentration for our subsequent antimicrobial drug. This concentration achieved high-efficiency bacterial clearance, while maintaining excellent cytocompatibility with negligible toxicity to mammalian skin cells, and avoided excessive temperature rise under near-infrared irradiation to prevent thermal damage to surrounding normal tissues, which fully meets the safety requirements of clinical wound treatment.

To systematically verify the “nanoknife” mechanical antibacterial effect of CI@MXene, first, gradient concentration antibacterial assays under complete dark conditions showed a significant concentration-dependent bactericidal activity of CI@MXene against both *E. coli* and *S. aureus*, with the colony number decreasing continuously as the material concentration increased, directly confirming the existence of contact-mediated mechanical damage (Figure S5). In Figure S6, ROS capture assays verified that CI@MXene did not produce sufficient ROS to exert effective antibacterial activity, excluding the contribution of oxidative stress to bacterial death. As show in Table S4, the metal dissolution results showed that in PBS solution, 200 µg/mL CI@MXene, 1.81 and 41.27 µg/L of Ti and Al were dissolved after 7 days. However, literature data shows that the concentrations of titanium ions and aluminum ions need to reach 4.5 mmol/L and 2% (v/v), respectively, to produce a certain antibacterial effect [41, 42]. Notably, compared with MXene, CI@MXene exhibited stronger antibacterial activity at the same concentration, indicating that the introduction of CI did not weaken but rather enhanced the nanoknife effect of MXene (Figure S7). This enhancement is likely attributed to the spatial barrier effect of CI molecules, which inhibits the stacking and agglomeration of MXene nanosheets, maintains the exposure of sharp edges, and improves the effective contact area with bacterial cell membranes, thus amplifying the mechanical puncture efficiency. These results collectively demonstrate that the enhanced antibacterial performance of CI@MXene in the dark is primarily driven by the reinforced nanoknife mechanical effect.

The fractional inhibitory concentration (FIC) index assay was performed to quantitatively evaluate the combined antibacterial effect of photothermal treatment and nanoknife-mediated mechanical bactericidal effect, following the standard guidelines of the Clinical and Laboratory Standards Institute. We selected CI@multilayer MXene, which has relatively weak mechanical antibacterial properties, as the photothermal-only group, and verified its lack of mechanical antibacterial activity through concentration gradient antibacterial experiments (Figure S8) [43]. As shown in Figure S9, Following the accepted criterion ($FIC<0.5 = \text{synergistic}, 0.5 \leq FIC \leq 1 = \text{additive}$), our results showed an $FIC = 120/800 + 120/600 = 0.35$ for *E. coli*, confirming a true synergistic effect. While $FIC = 150/800 + 150/400 = 0.56$ for *S. aureus*, indicating an additive effect. At the molecular and cellular levels, this combined effect is driven by the sequential complementary actions of the two mechanisms: mild photothermal heating increases bacterial membrane fluidity, reduces the mechanical rigidity of the peptidoglycan cell wall, suppresses bacterial stress repair capacity, and disrupts the biofilm extracellular matrix, which significantly lowers the threshold for MXene’s sharp edges to exert irreversible mechanical puncture (nanoknife effect) on bacteria, thus achieving the remarkable bactericidal and biofilm disruption efficacy we reported; the strain difference in FIC

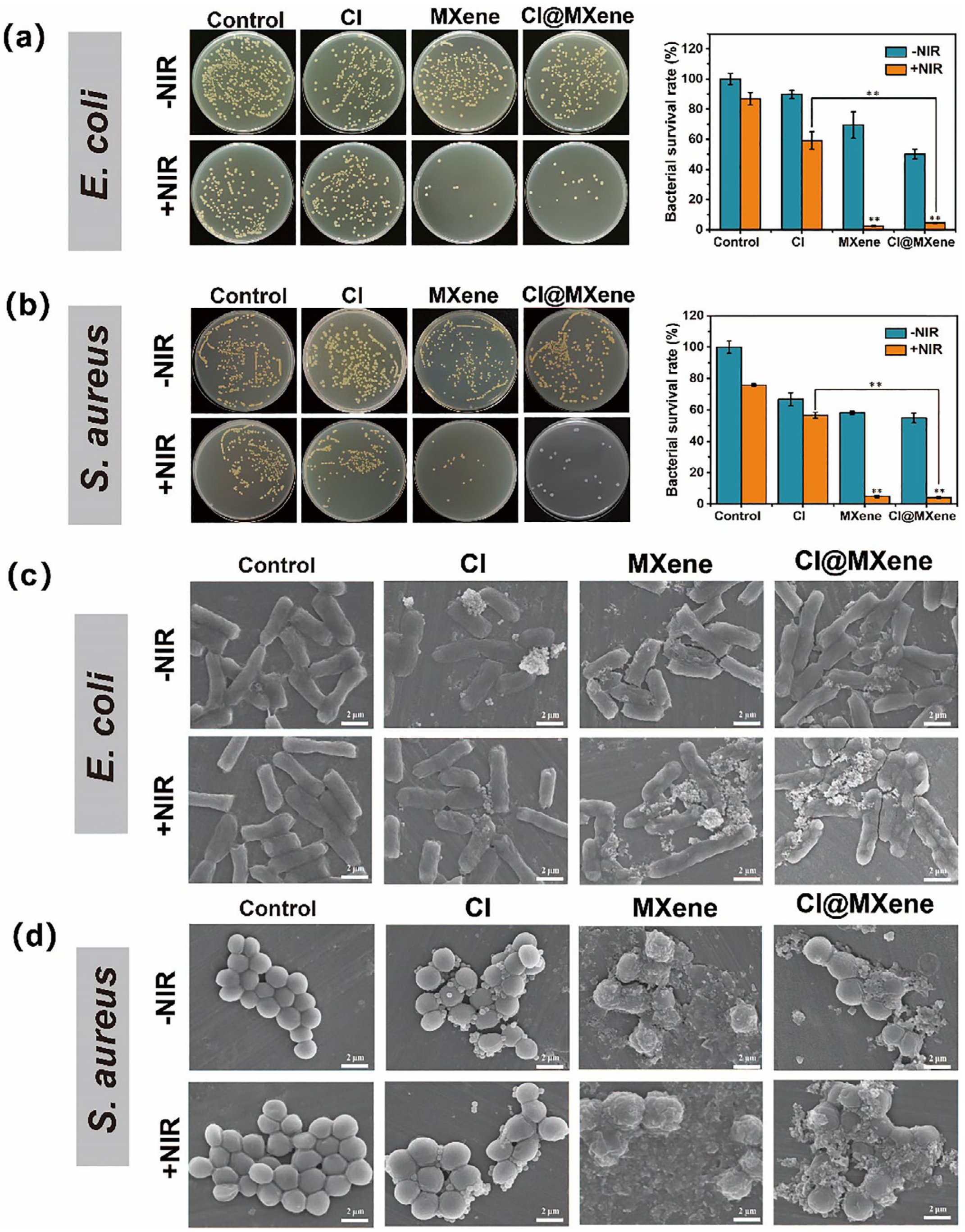

FIGURE 4 | The plate counts and the bacterial viability of (a) *E. coli* and (b) *S. aureus* with and without 808 nm NIR treatment, and the SEM images of (c) *E. coli*. And (d) *S. aureus*. after coculturing with Blank, CI, MXene and CI@MXene (120 μg/mL) with and without 808 nm NIR treatment. Data are presented as mean ± SD ($n = 4$). *$p < 0.05$, **$p < 0.01$, ***$p < 0.001$, ****$p < 0.0001$.

results is attributed to the thicker, more rigid peptidoglycan cell wall of Gram-positive *S. aureus*, which is less susceptible to photothermal-mediated structural weakening than the thin cell wall of Gram-negative *E. coli*.

Based on the favorable antibacterial performance of CI@MXene at a concentration of 120 μg/mL, its efficacy was compared against its individual precursors, CI and MXene. As shown in Figure 4a,b, with the NIR irradiation, CI showed negligible antibacterial activity relative to the blank control, whereas both MXene and CI@MXene reduced bacterial viability. CI@MXene demonstrated superior antibacterial efficacy (50%–60%) compared to CI and MXene, suggesting that the incorporation of CI does not significantly impair the "nanoknife" effect of MXene nanosheets. Under NIR irradiation, the antibacterial performance of both MXene and CI@MXene improved markedly, with the bacterial survival rates dropping to 2.4% and 4.5% respectively highlighting that the synergistic effect of photothermal and mechanical actions strengthened the sterilization capability. SEM was used to observe morphological changes in bacteria following different treatments. As depicted in Figure 4c, untreated *E. coli* in the blank group displayed a characteristic cylindrical shape with smooth, intact surfaces. After treatment with MXene or CI@MXene (without NIR), bacterial cells showed adhesion of material fragments, visible deformation, and membrane indentations. Following NIR irradiation, all material-treated groups induced more severe morphological damage. Notably, MXene and CI@MXene composites under photothermal treatment caused extensive bacterial shrinkage and membrane rupture. This damage is attributable to thermal disruption of bacterial membranes-composed primarily of lipids, proteins, and polysaccharides-as well as denaturation of intracellular DNA and proteins, ultimately leading to bacterial inactivation [44]. Figure 4d presents analogous morphological alterations in *S. aureus*. Due to their smaller size compared to *E. coli*, *S. aureus* cells were more inclined to be captured or encapsulated by MXene flakes, resulting in aggregate formation and physical membrane damage. Consequently, even without NIR irradiation, MXene-containing groups showed stronger antibacterial effects against *S. aureus* than against *E. coli*, consistent with previous reports [45]. Under NIR irradiation, *S. aureus* exhibited further structural ablation and severe deformation due to the combined mechanical and photothermal effects, reaffirming the outstanding synergistic bactericidal performance of the material across both Gram-positive and Gram-negative bacteria.

2.4 | Biofilm Ablation Capacity of CI@MXene

Biofilms, formed by bacteria encased within self-secreted extracellular matrices, significantly enhance bacterial resistance and are notably difficult to eradicate at infection sites [46]. Motivated by the notable photothermal sterilization capability of CI@MXene, we further investigated its anti-biofilm potential. *E. coli* and *S. aureus* biofilms were stained with SYTO 9 and PI and visualized using CLSM in 3D reconstruction mode. Live and dead bacteria were indicated by green and red fluorescence, respectively. As shown in Figure 5a, untreated bacterial biofilms remained structurally intact and uniformly fluorescent. After NIR irradiation, the control group showed limited bacterial damage, with dominant green fluorescence indicating high viability. In contrast, the material-treated groups exhibited anti-biofilm effects correlated with their photothermal performance: the CI group showed yellow fluorescence, suggesting a mixed population of live and dead bacteria; the MXene group exhibited reddish-yellow fluorescence due to an increased ratio of dead cells; and the CI@MXene group displayed strong red fluorescence, indicating extensive bacterial death. To quantitatively support the CLSM observations, biofilm biomass was measured using crystal violet staining. As shown in Figure 5b,c, the non-NIR treated control group showed intense purple staining, indicating dense biofilm formation. While CI alone had little inhibitory effect, both MXene and CI@MXene reduced biofilm formation, with inhibition rates of 52.2% and 42.4%, respectively. Under NIR irradiation, the anti-biofilm performance of all materials improved significantly. The MXene and CI@MXene groups, which displayed strong photothermal effects, showed nearly complete elimination of biofilm, with inhibition rates of 73.9% and 71.7% for *E. coli*, and 76.9% and 78.5% for *S. aureus*, respectively. These crystal violet results are consistent with the CLSM data, confirming that the CI@MXene composite effectively inhibits both biofilm formation and growth.

Additionally, to evaluate the antibacterial efficacy of the composite against biofilm-embedded bacteria, the viability of residual bacteria within the biofilms was assessed using SYTO 9/PI staining and plate-counting methods. Under NIR irradiation, CLSM imaging revealed that both MXene and CI@MXene exhibit photothermal and mechanical effects, resulting in enhanced antibacterial properties that are induced predominantly red fluorescence in the remaining biofilm bacteria, indicating a high proportion of dead cells. The number of non-viable bacteria in these groups was consistently higher than in other treatment conditions (Figure 5d). These results confirm that the photothermal-mechanical synergistic antibacterial action of the CI@MXene composite not restrains biofilm formation and development, but also effectively eliminates bacteria within mature biofilms, resulting in highly efficient anti-biofilm performance.

2.5 | Biocompatibility Evaluation

Ideal biocompatibility is a critical requirement for the biological application of materials. As shown in Figure S10(a–c), all materials exhibited concentration-dependent cytotoxicity, with cell viability decreasing as material concentration increased. Notably, MXene showed the most significant cytotoxicity among the three materials: at the highest tested concentration of 200 µg/mL, the cell viability was only 64.2% for HUVECs, 76.5% for NIH-3T3 and 79.8% for RAW 264.7. In contrast, CI maintained excellent biocompatibility across all tested concentrations, with cell viability remaining above 85% even at 200 µg/mL. Impressively, the CI@MXene composite exhibited significantly improved cytocompatibility compared to MXene: at 200 µg/mL, the cell viability was 82.3% for HUVECs, 89.1% for NIH-3T3 fibroblasts and 90.2% for RAW 264.7 macrophages, which was comparable to CI and far superior to MXene.

Furthermore, we evaluated the photothermal cytotoxicity of different materials against RAW 264.7 macrophages under the same NIR irradiation parameters used for antibacterial treatment (Figure S10d). After NIR irradiation, MXene showed the most dramatic decrease in cell viability from 80.1% to 58.7%, which is attributed to its excessive temperature rise. In contrast, CI@MXene maintained a much higher cell viability of 74.3% after NIR irradiation, with only a 12.9% decrease compared to the dark condition, confirming its excellent biocompatibility under therapeutic photothermal conditions. The mild photothermal effect of CI@MXene further ensures its safety during in vivo treatment, avoiding the thermal damage to surrounding normal tissues that is commonly associated with conventional photothermal agents [47–49].

Materials with poor blood compatibility can induce hemolysis, resulting in the release of hemoglobin into the supernatant and raising significant biosafety concerns. Hemolysis assays were performed using sterile defibrinated sheep blood, with Triton X-100 and PBS serving as the positive and negative controls, respectively. As shown in Figure S11a, the hemolysis rate of CI@MXene at a concentration of 1000 µg/mL was 0.68%, which is below the internationally recognized safety threshold of 2%. Corresponding photographs in Figure S11b confirm that CI@MXene induced no observable hemolysis. The mechanical force from CI@MXene can effectively puncture the rigid peptidoglycan cell wall of

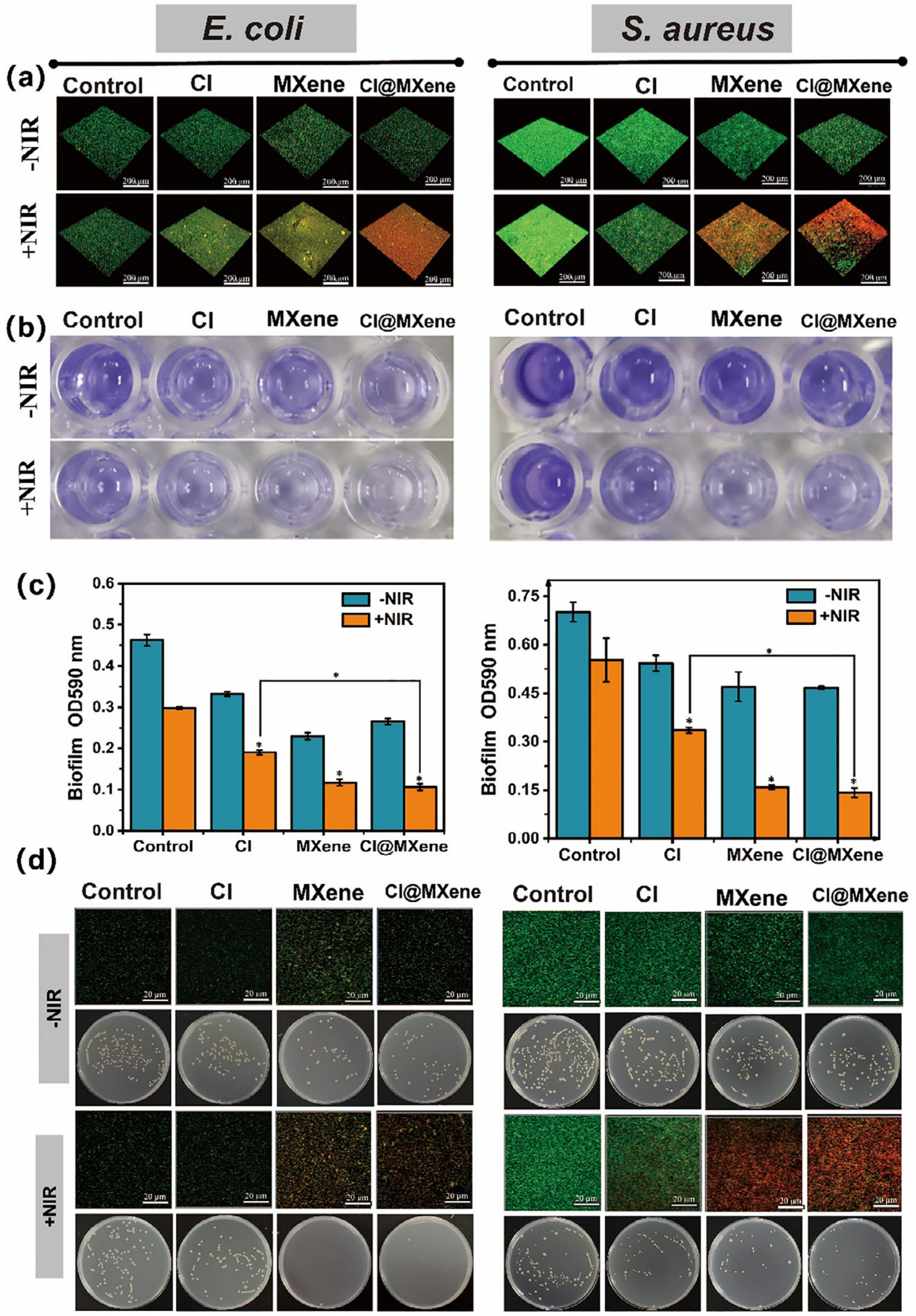

FIGURE 5 | In vitro anti-biofilm efficacy of CI@MXene. (a) Representative CLSM images of biofilms stained with the LIVE/ DEAD ™ BacLight kit (green: live bacteria; red: dead bacteria). (b) Crystalline violet staining of mature biofilms after treatment. (c) Quantitative analysis of biofilm biomass reduction. (d) Fluorescence imaging of SYTO 9/PI staining and corresponding diluted plate counts of the viable bacteria. Data are presented as mean ± SD ($n = 4$). $^{*}p < 0.05$, $^{**}p < 0.01$, $^{***}p < 0.001$, $^{****}p < 0.0001$.

bacteria (Young's modulus of 1-–20 GPa) to exert bactericidal activity, but is insufficient to cause irreversible damage to the highly flexible mammalian erythrocyte membrane, which has a Young's modulus of only a few hundred pascals (5–6 orders of magnitude lower than that of bacterial cell walls) [50–52]. These results demonstrate the material's robust hemocompatibility, a crucial property for its further development in biomedical applications and potential clinical translation.

2.6 | In Vivo Wound Healing Performance of CI@MXene

A wound model infected with *S. aureus* was established to evaluate the wound healing efficacy of CI@MXene in vivo. As the treatment progressed, all groups exhibited varying degrees of wound closure, as depicted in Figure 6a. From day 5 onward, the CI, MXene, and CI@MXene composite groups showed a tendency

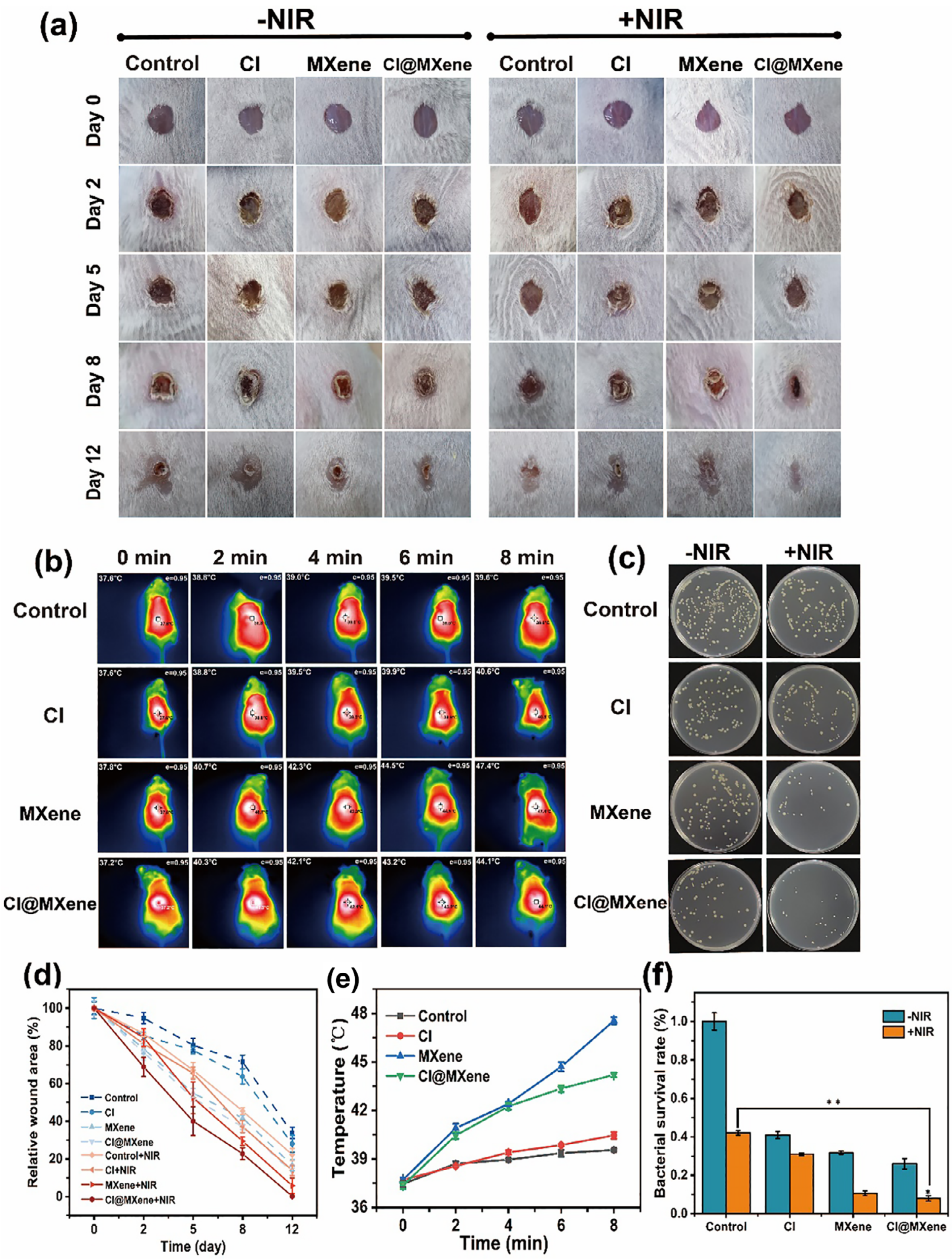

FIGURE 6 | (a) Representative photographic images of *S. aureus*-infected wounds. (b) Thermal images of wounds during NIR treatment. (c) Colony-forming unit (CFU) counts of bacteria extracted from wound tissues. (d) Quantitative analysis of wound area of mice in each treatment group. (e) Temperature changes of the wounds during NIR treatment. (f) Bacterial viability of the Residual bacterial. Data are presented as mean ± SD ($n = 6$). $^{*}p < 0.05$, $^{**}p < 0.01$, $^{***}p < 0.001$, $^{****}p < 0.0001$.

toward scab formation. By day 8, pronounced differences in wound area were observed among the groups. The CI, MXene, and CI@MXene groups without NIR irradiation displayed noticeable scabbing, whereas those receiving NIR treatment exhibited reduced wound areas. Among these, the NIR-treated CI@MXene group demonstrated significantly accelerated wound healing compared to all other groups. By day 12, the wounds in the NIR-treated CI@MXene group were almost completely healed. As quantified in Figure 6d, the CI@MXene and MXene groups receiving NIR exhibited accelerated healing trends beginning on day 2, with a pronounced improvement between day 2 and 5. The CI@MXene (+NIR) group showed particularly superior wound-healing effects. Notably, even in the absence of NIR, the CI@MXene and MXene groups achieved therapeutic outcomes comparable to-and those on the day 5 with NIR exposure, superior to-those of the NIR-treated Blank and CI groups. These results suggest that the intrinsic mechanical antibacterial properties of the material effectively facilitate healing in bacterial-infected wounds. Throughout the treatment period, mouse body weights were recorded every other day. As shown in Figure S12, aside from a slight weight loss immediately following wound modeling, subsequent body weights recovered and remained stable. This transient weight loss was likely attributable to reduced appetite and activity levels resulting from wound-induced stress.

Under NIR irradiation, excessive whole-body temperature elevation had adverse effects on the normal tissues of mice. We therefore recorded infrared thermal images of mice to monitor temperature changes at the wound site over an 8 min irradiation period. As shown in Figure 6b,e, the temperature in both the CI@MXene and MXene groups rapidly increased to 40.0°C within 2 min of irradiation. After 8 min, the temperature of the CI@MXene group stabilized at 44.1°C, which was higher than that of the MXene group. The mild photothermal effect mediated by CI@MXene not only effectively eliminated infectious bacteria at the wound site but also promoted the healing of wound tissue. Compared with traditional high-temperature photothermal therapy, this approach avoids damage to surrounding tissues, achieving superior wound treatment superior. Quantitative analysis of bacteria collected from wound tissue on day 12 (Figure 6c,f) showed that the antibacterial effect was enhanced in all groups following near-infrared irradiation. In the CI@MXene group, the bacterial count was significantly reduced by 91.2%. This 91.2% reduction in bacterial count effectively lowered the bacterial load below the host immune clearance threshold. The remaining bacteria could be efficiently phagocytosed and eliminated by macrophages and neutrophils recruited to the wound site, preventing proliferation and recurrent infection [53–55]. This further confirms that the composite material exhibits superior photothermal synergistic antibacterial performance compared to MXene. These results demonstrate that the CI@MXene composite combats *S. aureus* infection effectively in mouse wounds.

2.7 | Histological Evaluation

On day 12 post-wounding, wound tissue and adjacent normal skin were harvested from mice and subjected to H&E staining. Histological analysis was conducted across the negative control group and various treatment groups to evaluate the biological effects of the samples on *S. aureus*-infected wound model. As observed in Figure 7a, the Blank group without NIR irradiation remained in the inflammatory phase on day 12, displaying mild epidermal damage and intercellular edema. In contrast, all sample-treated groups showed reduced inflammatory cell infiltration. Notably, the CI@MXene group exhibited mild repair of the damaged dermal tissue architecture. After NIR irradiation, as illustrated in Figure 7b, a further reduction in inflammatory cells was observed in all treated groups. Importantly, both the MXene and CI@MXene groups showed no significant inflammatory cell aggregation, with most tissues and cells presenting normal morphology. Magnified images revealed intact hair follicles, epidermis, and dermis. These results suggest that CI@MXene shortens the inflammatory phase effectively and promotes regeneration of epidermal tissue rapidly, demonstrating considerable wound-healing efficacy.

3 | Conclusions

A straightforward method for preparing a natural melanin/MXene composite (CI@MXene) has been developed in this work. Systematic evaluations confirmed the remarkable oxidative stability of CI@MXene in aqueous environments, maintaining structural integrity even after 40 days of storage, along with a high photothermal conversion efficiency of 42.1%. Under NIR irradiation, the composite effectively inactivated *E. coli* and *S. aureus* and disrupted approximately 80% of established biofilms through synergistic photothermal-mechanical action. Cytotoxicity assays further revealed that the incorporation of CI significantly improved the biocompatibility of MXene. In vivo experiments demonstrated that CI@MXene treatment markedly accelerated the healing of bacterial-infected wounds, underscoring its strong antibacterial and anti-inflammatory capabilities in practical wound management. Thus, the CI@MXene composite, with its integrated advantages of enhanced stability, excellent biocompatibility, and effective wound-healing performance, offers a promising strategy for broadening the biomedical application of MXene-based nanomaterials.

4 | Experimental Section

4.1 | Chemicals and Reagents

Ti_3AlC_2 was obtained from Jilin Province Yiyi Technology Co., Ltd.; cuttlefish ink was sourced from cuttlefish ink sacs in Qingdao, Shandong Province; lithium fluoride (LiF) was supplied by Aladdin Reagent Co., Ltd.; hydrochloric acid (HCl), glacial acetic acid (CH_3COOH), crystal violet (CV), and anhydrous ethanol (EtOH) were provided by Tianjin Damiao Chemical Reagent Factory; LB medium and technical agar powder were bought from Guangdong Huankai Microbial Technology Co., Ltd.; SYTO 9 green dye and propidium iodide (PI) were purchased from Thermo Fisher Scientific (China) Co., Ltd.; DMEM high-glucose medium was sourced from Gibco; 1X PBS buffer solution, penicillin-streptomycin solution (100X dual antibiotic), 4% paraformaldehyde, and mouse fibroblast cells (NIH-3T3) were supplied by Biosharp Biotechnology Co., Ltd.; fetal bovine serum was sourced from RAR.

4.2 | Preparation of CI@MXene

4.2.1 | Extraction of Cuttlefish Ink Melanin

Fresh CI was extracted from cuttlefish ink sacs following a previously reported method with modifications [28]. Briefly, 20 g of cuttlefish ink sac juice was mixed with 80 g of an EtOH-water mixture (1:1, v/v). The mixture was stirred thoroughly and stored at 4.0°C overnight. The resulting suspension was then centrifuged at 4000 rpm for 10 min, and the supernatant was discarded. The precipitate was redispersed in deionized (DI)

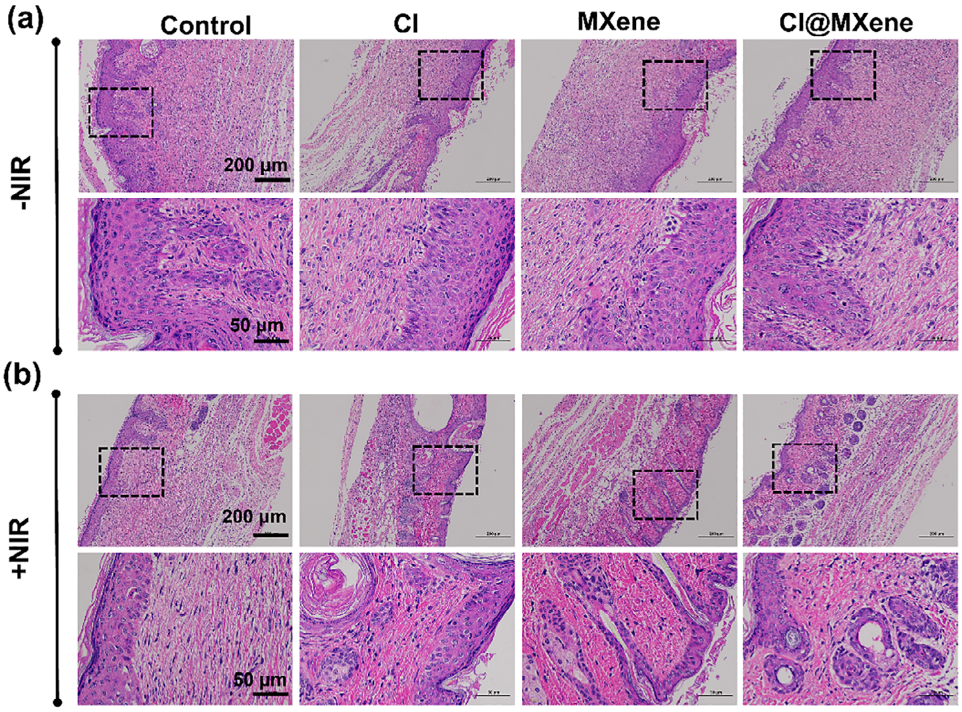

FIGURE 7 | H&E histological staining of mouse wound sections (a) without NIR and (b) with NIR treatment after 12 days Images are shown at two different magnifications.

water, and the washing process was repeated 2–-3 times. Finally, the collected precipitate was dried in an oven at 60.0°C and ground into a fine black CI powder.

4.2.2 | Preparation of CI@MXene

Thin-layer MXene was synthesized by selectively etching the aluminum layer from Ti_3AlC_2 using a LiF/HCl mixture according to a previously reported method with modifications [56]. Briefly, 40 mL HCl of 9 M and 2 g LiF were added to a polytetrafluoroethylene beaker and stirred at 400 rpm for 30 min. Then, 2 g of Ti_3AlC_2 powder was gradually added to the mixture, which was maintained at 35.0°C for 24 h under continuous stirring to allow complete etching. The resulting suspension was centrifuged at 3500 rpm for 10 min. Retained the precipitate, redispersed it with DI water, and sonicated for 10 min. This washing process was repeated until the supernatant reached a pH of 6 approximately. Subsequently, 40 mL of EtOH was added, and the mixture was sonicated for 1 h to promote delamination. After centrifugation at 10 000 rpm for 10 min, the precipitate was redispersed in DI water, and sonicated for 20 min. The suspension was then centrifuged at 3500 rpm for 3 min to collect the supernatant, which was freeze-dried to obtain monolayer MXene.

To prepare the CI@MXene composite, 50 mL of MXene aqueous dispersion (0.4 mg/mL) and 50 mL of CI aqueous solution (0.04 mg/mL) were separately sonicated for 40 min. The two dispersions were then combined in a 150 mL beaker and stirred at 400 rpm at room temperature for 1 h. Centrifuged the resulting mixture twice (3500 rpm, 5 min) to collect the solid product. And vacuum-dried it at 60.0°C for 24 h to obtain the final black CI@MXene powder.

4.3 | Physical Characterization

The microstructure and morphology of the materials were characterized using transmission electron microscopy (TEM; Hitachi HT7700, Japan) and field-emission scanning electron microscopy (FESEM; Talos F200S, Czech Republic). Elemental distribution was analyzed by energy-dispersive x-ray spectroscopy (EDX) coupled with FESEM. Functional groups were identified using a Fourier transform infrared spectrometer (FTIR; Nicolet 6700, USA). Crystallographic structures were examined by x-ray diffraction (XRD; Rigaku Ultima IV, Japan). Surface elemental composition and chemical states were determined by x-ray photoelectron spectroscopy (XPS; Thermo Scientific K-Alpha, USA). Biofilm morphology was visualized using confocal laser scanning microscopy (CLSM; ZEISS LSM800 with Airyscan, Germany). Histological sections of mouse wound tissues were observed under an optical microscope (Nikon Eclipse E100, Japan). The photothermal performance was evaluated using an 808 nm near-infrared laser (LDP-808, China). The photothermal conversion efficiency (η) of each material was calculated according to the following equation [57, 58]:

$$\eta = \frac{hS\,(T_{max} - T_{surr}) - Q_0}{I\left(1 - 10^{-A_{808}}\right)} \tag{1}$$

$$\tau_s = \frac{m_d C_d}{hS} \tag{2}$$

$$Q_0 = hS\left(T_{max,water} - T_{surr}\right) \tag{3}$$

Here, T_{max} and T_{surr} denote the maximum temperature and room temperature, respectively. I represents the laser power. A_{808} is the ultraviolet absorption value of the sample at 808 nm. τ_s is the heat transfer coefficient. m_d and C_d denote the mass of the solution and the specific heat capacity of the solvent, respectively.

4.4 | In Vitro Antibacterial Experiment

Gram-negative (*E. coli*, ATCC 25922) and Gram-positive (*S. aureus*, ATCC 25923) were selected as model bacterial strains. Before each experiment, 200 µL of frozen stock culture of each bacterium was inoculated into 10 mL of LB liquid medium and incubated at 37.0°C in a shaking incubator at 200 rpm for 8–12 h. The bacterial cells were then harvested, washed with sterile physiological saline, and adjusted to a concentration of 5×10^6 CFU/mL. Subsequently, 120 µL of LB medium, 40 µL of sample solution, and 40 µL of bacterial suspension (5×10^6 CFU/mL) were mixed in a 96-well plate and incubated at 37.0°C with shaking at 200 rpm for 1 h. After incubation, the mixtures were either exposed or not exposed to 808 nm laser irradiation at a power density of 1.5 W/cm^2 for 8 min. The treated bacterial suspensions were then serially diluted to 10^4 CFU/mL, and 50 µL of each dilution was spread onto LB agar plates. After incubation at 37.0°C for 12–24 h, the number of colonies was counted to determine antibacterial activity.

$$\text{FIC Index } = \frac{MIC\ of\ CI@MXene\,(nanoknife + NIR)}{MIC\ of\ CI@multilayerMXene\,(NIR)} + \frac{MIC\ of\ CI@MXene\,(nanoknife + NIR)}{MIC\ of\ CI@MXene\,(nanoknife)} \quad (4)$$

The widely recognized criterion for combined effect classification was adopted: FIC index < 0.5 indicates a significant synergistic effect; 0.5 ≤ FIC index ≤ 1 indicates an additive effect; FIC index > 1 indicates an antagonistic effect. All experiments were performed in 6 biological replicates.

4.5 | Antibiofilm Experiment

200 µL of *E. coli* or *S. aureus* suspension (10^7 CFU/mL) in the logarithmic growth phase was combined with 800 µL of LB in a 24-well plate. The plate was incubated statically at 37.0°C for 48 h. Then, each well was gently washed with 1 × PBS buffer to remove non-adherent cells. 1 mL of sample solution (120 µg/mL) was added to each well. Selected wells were subjected to NIR irradiation for 8 min, while non-irradiated wells served as controls. After treatment, the solution was carefully aspirated using a syringe. The wells were rinsed again with 1 × PBS, followed by fixation with 1 mL of methanol for 20 min. The methanol was then removed, and the plate was air-dried completely. Biofilms were stained with 1 mL of 0.1% CV for 15 min, followed by removing the excess dye through washing 2–-3 times with 1 × PBS. Finally, the bound dye was dissolved using 1 mL of 33% CH_3OOH solution for 10 min. The plate was shaken for 2 min to ensure complete dissolution, and the absorbance of the solution was measured at 590 nm.

4.6 | Cytotoxicity Evaluation

The MTT assay was performed to assess the biocompatibility of the composite material. First, cells were resuspended following centrifugation, diluted to an appropriate concentration, and counted. Then based on the counting results, the cell density was adjusted to 5×10^3 cells per well in a 96-well plate and incubated at 37.0°C in a 5% CO_2 atmosphere for 24 h. After incubation, the original culture medium was aspirated and replaced with DMEM dispersions containing the three test materials at various concentrations. The cells were then incubated for another 24 h. Subsequently, the material dispersions were removed, and the cells were gently rinsed 2–-3 times with 1 × PBS. Then, 100 µL of MTT solution (0.5 mg/mL) was added to each well, and the plate was incubated in the dark for 3 h. The MTT solution was then carefully aspirated, and 100 µL of DMSO was added to each well to dissolve the formazan crystals. The absorbance was measured at 570 nm.

4.7 | Hemolysis Assay

Evaluate the blood compatibility of CI@MXene using defibrinated sheep blood. Add 1 mL of fresh blood to 8 mL of PBS, centrifuge at 2000 rpm for 10 min, remove the supernatant, and wash the precipitate 2–-3 times with PBS. Resuspend the red blood cell precipitate to form a 5% red blood cell suspension. In a 1.5 mL centrifuge tube, combine 500 µL of the suspension with 500 µL of CI@MXene solution at different concentrations. Incubate at 37.0°C for 1 h, then centrifuge to collect the supernatant. Measure its absorbance at 540 nm. Triton X-100 and PBS served as positive and negative controls, respectively.

4.8 | In Vivo Experiments

An animal model of bacterial wound infection was established to evaluate the antibacterial and wound-healing efficacy of the materials. All animal experiments were approved by Shenzhen TopBiotech Co.,Ltd (Approval Number: TOP-IACUC-2022-0233). Female Balb/c mice aged six to eight weeks (average weight 18–-22 g) were acclimatized for one week with free access to food and water, and bedding was changed every two days. After intraperitoneal anesthesia, the dorsal skin was shaved and cleaned using a razor and hair removal cream. Once the cream was removed, the skin was gently lifted, and a full-thickness wound with a diameter of 5 mm was created using a biopsy punch. Each wound was inoculated with 50 µL of *S. aureus* suspension (1×10^8 CFU/mL) to ensure complete coverage of the wound area. After 24 h, the mice were randomly divided into a blank control group (Blank) and several experimental groups, including corresponding NIR treatment subgroups. Mice in the NIR-treated groups were exposed to an 808 nm laser at a power density of 1.5 W/cm^2 for 8 min (designated as Day 1). Infrared thermal imaging was performed during irradiation to monitor temperature changes at the wound site. The wound area and body weight of each mouse were recorded every other day. Wound areas were measured and analyzed using ImageJ software. On Day 12, all mice were euthanized, and wound tissues were harvested for dehydration, paraffin embedding, sectioning, and staining. Histological evaluation was carried out using optical microscopy.

4.9 | Statistical Analysis

All data are expressed as mean ± standard deviation (SD). t-tests were performed using Origin 2019b software, where * denotes $p < 0.05$, ** denotes $p < 0.01$, and *** denotes $p < 0.001$. Results above these thresholds are considered statistically significant.

Author Contributions

Zhenxing Tan: Data curation, Methodology, Investigation, Formal analysis, Writing – original draft. **Xiaotong Huang**: Data curation, Investigation, Formal analysis, Visualization. **Dandan Zhang**: Investigation, Methodology. **Hao Huang**: Data curation. **Rongrong Hu**: Investigation. **Caijie Ding**: Investigation. **Wenxia Wang**: Methodology, Investigation, Supervision, Writing – review & editing. **Yong Yuan**: Supervision, Writing – review & editing. **Lihua Zhou**: Funding acquisition, Investigation, Resources, Methodology Writing – original & editing.

Acknowledgements

This work was financially supported by the National Natural Science Foundation of China (Nos. 42277023 and 42477256).

Conflicts of Interest

The authors declare no conflicts of interest.

Data Availability Statement

Data will be made available on request.

References

1. S. Darvishi, S. Tavakoli, M. Kharaziha, H. Girault, C. Kaminski, and I. Mela, "Advances in the Sensing and Treatment of Wound Biofilms," *Angewandte Chemie International Edition* 61, no. 13 (2022): 202112218, https://doi.org/10.1002/anie.202112218.

2. M. Li, C. Wang, Q. Yu, et al., "A Wearable and Stretchable Dual-Wavelength LED Device for Home Care of Chronic Infected Wounds," *Nature Communications* 15, no. 1 (2024): 9380, https://doi.org/10.1038/s41467-024-53579-6.

3. P. Virych, O. Nadtoka, V. Doroschuk, et al., "Cefuroxime-Loaded Hydrogels for Prevention and Treatment of Bacterial Contamination of Open Wounds," *International Journal of Polymer Science* 2021 (2021): 1–7, https://doi.org/10.1155/2021/4935642.

4. R. Ranjbar and M. Alam, "Antimicrobial Resistance Collaborators (2022). Global Burden of Bacterial Antimicrobial Resistance in 2019: A Systematic Analysis," *Evidence-based nursing* 399, no. 10325 (2023): 629–655, https://doi.org/10.1136/ebnurs-2022-103540.

5. V. Band, D. Hufnagel, S. Jaggavarapu, et al., "Antibiotic Combinations That Exploit Heteroresistance to Multiple Drugs Effectively Control Infection," *Nature Microbiology* 4, no. 10 (2019): 1627–1635, https://doi.org/10.1038/s41564-019-0480-z.

6. F. Wu, H. Zheng, W. Wang, et al., "Rapid Eradication of Antibiotic-Resistant Bacteria and Biofilms by MXene and Near-Infrared Light Through Photothermal Ablation," *Science China Materials* 64, no. 3 (2021): 748–758, https://doi.org/10.1007/s40843-020-1451-7.

7. S. Hao, H. Han, and Z. Yang, "Recent Advancements on Photothermal Conversion and Antibacterial Applications Over MXenes-Based Materials," *Nano-Micro Letters* 14, no. 1 (2022): 178, https://doi.org/10.1007/s40820-022-00901-w.

8. W. Wang, Y. Huang, Y. Zhang, et al., "Research Progress of Multifunctional Inorganic Nanomaterials for Tumor Photothermal Therapy," *Nanoscale* 17 (2025): 21938–21960, https://doi.org/10.1039/D5NR02839F.

9. A. Rozmyslowska-Wojciechowska, E. Karwowska, S. Pozniak, et al., "Influence of Modification of Ti_3C_2 MXene With Ceramic Oxide and Noble Metal Nanoparticles on its Antimicrobial Properties and Ecotoxicity Towards Selected Algae and Higher Plants," *RSC Advances* 9, no. 8 (2019): 4092–4105, https://doi.org/10.1039/c8ra07633b.

10. Y. Liu, Y. Tian, Q. Han, et al., "Synergism of 2D/1D MXene/Cobalt Nanowire Heterojunctions for Boosted Photo-Activated Antibacterial Application," *Chemical Engineering Journal* 410 (2021): 128209, https://doi.org/10.1016/j.cej.2020.128209.

11. M. Overchuk, R. A. Weersink, B. C. Wilson, and G. Zheng, "Photodynamic and Photothermal Therapies: Synergy Opportunities for Nanomedicine," *ACS Nano* 17, no. 9 (2023): 7979–8003, https://doi.org/10.1021/acsnano.3c00891.

12. W. Wang, D. Luo, Y. Huang, et al., "One Arrow Two Eagles: Design and Synthesis of "All-In-One" Nanoscale Cu-IR825 Nanoparticles for Photothermally Augmented Chemodynamic Therapy," *Materials Chemistry Frontiers* 10 (2026): 1133–1146, https://doi.org/10.1039/D5QM00881F.

13. L. Chen, M. Wakeel, T. Ul Haq, N. S. Alharbi, C. Chen, and X. Ren, "Recent Progress in Environmental Remediation, Colloidal Behavior and Biological Effects of MXene: A Review," *Environmental Science: Nano* 9, no. 9 (2022): 3168–3205, https://doi.org/10.1039/d2en00340f.

14. H. Lin, Y. Wang, S. Gao, Y. Chen, and J. Shi, "Theranostic 2D Tantalum Carbide (MXene)," *Advanced Materials* 30, no. 4 (2017): 1703284, https://doi.org/10.1002/adma.201703284.

15. G. Liu, Q. Xiong, Y. Xu, et al., "Magnetically Separable MXene@Fe_3O_4/Au/PDA Nanosheets With Photothermal-Magnetolytic Coupling Antibacterial Performance," *Applied Surface Science* 590 (2022): 153125, https://doi.org/10.1016/j.apsusc.2022.153125.

16. K. A. M. Xavier, V. Geethalekshmi, S. R. Senapati, P. T. Mathew, A. C. Joseph, and K. G. R. Nair, "Valorization of Squid Processing Waste as Animal Feed Ingredient by Acid Ensilaging Process," *Waste and Biomass Valorization* 8, no. 6 (2017): 2009–2015, https://doi.org/10.1007/s12649-016-9764-1.

17. Y. Liu and J. Simon, "Metal–Ion Interactions and the Structural Organization of Sepia Eumelanin," *Pigment Cell Research* 18, no. 1 (2005): 42–48, https://doi.org/10.1111/j.1600-0749.2004.00197.x.

18. C.-H. Xue, H.-G. Li, X.-J. Guo, et al., "Superhydrophobic Anti-Icing Coatings With Self-Deicing Property Using Melanin Nanoparticles From Cuttlefish Juice," *Chemical Engineering Journal* 424 (2021): 130553, https://doi.org/10.1016/j.cej.2021.130553.

19. J. Xie, H. Li, H. Che, X. Dong, X. Yang, and W. Xie, "Extraction, Physicochemical Characterisation, and Bioactive Properties of ink melanin From Cuttlefish (*Sepia* Esculenta)," *International Journal of Food Science & Technology* 56, no. 7 (2021): 3627–3640, https://doi.org/10.1111/ijfs.14992.

20. Y.-S. Kwon, M. Zheng, A. Y. Zhang, and Z. Han, "Melanin-Like Nanoparticles as an Alternative to Natural Melanin in Retinal Pigment Epithelium Cells and Their Therapeutic Effects Against Age-Related Macular Degeneration," *ACS Nano* 16, no. 11 (2022): 19412–19422, https://doi.org/10.1021/acsnano.2c09087.

21. W. Dong, Y. Wang, C. Huang, et al., "Enhanced Thermal Stability of Poly (Vinyl Alcohol) in Presence of Melanin," *Journal of Thermal Analysis and Calorimetry* 115, no. 2 (2014): 1661–1668, https://doi.org/10.1007/s10973-013-3419-2.

22. P. Kumar, M. Kannan, V. ArunPrasanna, B. Vaseeharan, and S. Vijayakumar, "Proteomics Analysis of Crude Squid Ink Isolated From *Sepia* Esculenta for Their Antimicrobial, Antibiofilm and Cytotoxic Properties," *Microbial Pathogenesis* 116 (2018): 345–350, https://doi.org/10.1016/j.micpath.2018.01.039.

23. Y. Zhang, Q. Wang, Y. Ji, et al., "Mitochondrial Targeted Melanin@mSiO$_2$ Yolk-Shell Nanostructures for NIR-II-Driven Photo-Thermal-Dynamic/Immunotherapy," *Chemical Engineering Journal* 435 (2022): 134869, https://doi.org/10.1016/j.cej.2022.134869.

24. Q. Jiang, Z. Luo, Y. Men, et al., "Red Blood Cell Membrane-Camouflaged Melanin Nanoparticles for Enhanced Photothermal Therapy," *Biomaterials* 143 (2017): 29–45, https://doi.org/10.1016/j.biomaterials.2017.07.027.

25. C. Xue, H. Li, X. Guo, et al., "Superhydrophobic Anti-Icing Coatings With Self-Deicing Property Using Melanin Nanoparticles From Cuttlefish Juice," *Chemical Engineering Journal* 424 (2021): 130553, https://doi.org/10.1016/j.cej.2021.130553.

26. K. Wang, Y. Hou, B. Poudel, et al., "Melanin–Perovskite Composites for Photothermal Conversion," *Advanced Energy Materials* 9, no. 9 (2019): 1901753, https://doi.org/10.1002/aenm.201901753.

27. W. Wang, Y. Huang, Y. Li, et al., "Multifunctional Metal-Organic Frameworks and Their Heterojunction Materials for Cancer Theranostics," *Bio Sci* 13 (2025): 4081–4096, https://doi.org/10.1039/D5BM00544B.

28. X. Huang, C. Yang, Y. Chen, Z. Zhu, and L. Zhou, "Cuttlefish Ink-Based N and S Co-Doped Carbon Quantum Dots as a Fluorescent Sensor for Highly Sensitive and Selective *Para*-Nitrophenol Detection," *Analytical Methods* 13, no. 44 (2021): 5351–5359, https://doi.org/10.1039/d1ay01496j.

29. W.-T. Cao, F.-F. Chen, Y.-J. Zhu, et al., "Binary Strengthening and Toughening of MXene/Cellulose Nanofiber Composite Paper With Nacre-Inspired Structure and Superior Electromagnetic Interference Shielding Properties," *ACS Nano* 12, no. 5 (2018): 4583–4593, https://doi.org/10.1021/acsnano.8b00997.

30. B. Ahmed, D. H. Anjum, Y. Gogotsi, and H. N. Alshareef, "Atomic Layer Deposition of SnO$_2$ on MXene for Li-Ion Battery Anodes," *Nano Energy* 34 (2017): 249–256, https://doi.org/10.1016/j.nanoen.2017.02.043.

31. X. Li, G. Fan, and C. Zeng, "Synthesis of Ruthenium Nanoparticles Deposited on Graphene-Like Transition Metal Carbide as an Effective Catalyst for the Hydrolysis of Sodium Borohydride," *International Journal of Hydrogen Energy* 39, no. 27 (2014): 14927–14934, https://doi.org/10.1016/j.ijhydene.2014.07.029.

32. M. Peng, L. Wang, and L. Li, "Manipulating the Interlayer Spacing of 3D MXenes With Improved Stability and Zinc-Ion Storage Capability," *Advanced Functional Materials* 32, no. 7 (2021): 2109524, https://doi.org/10.1002/adfm.202109524.

33. J. Shan, X. Zhang, and Y. Cheng, "Glucose Metabolism-Inspired Catalytic Patches for NIR-II Phototherapy of Diabetic Wound Infection," *Acta Biomaterialia* 157 (2023): 200–209, https://doi.org/10.1016/j.actbio.2022.12.001.

34. M. Wang, M. Chang, Q. Chen, et al., "Au$_2$Pt-PEG-Ce6 nanoformulation With Dual Nanozyme Activities for Synergistic Chemodynamic Therapy / Phototherapy," *Biomaterials* 252 (2020): 120093, https://doi.org/10.1016/j.biomaterials.2020.120093.

35. C. M. Hessel, V. P. Pattani, M. Rasch, et al., "Copper Selenide Nanocrystals for Photothermal Therapy," *Nano Letters* 11, no. 6 (2011): 2560–2566, https://doi.org/10.1021/nl201400z.

36. M. Salimi, M. A. Shokrgozar, D. H. Hamid, and M. Vossoughi, "Photothermal Properties of Two-Dimensional Molybdenum Disulfide (MoS$_2$) With Nanoflower and Nanosheet Morphology," *Materials Research Bulletin* 152 (2022): 111837, https://doi.org/10.1016/j.materresbull.2022.111837.

37. N. Alduhisan, A. AL-Zahrani, Y. AL-Zahrani, et al., "Investigation of the Influence of Calcination Temperature on the Photocatalytic Performance of TiO$_2$ Nanotubes Doped With Ti$_3$C$_2$T$_x$ MXene," *Surfaces and Interfaces* 78 (2025): 108097, https://doi.org/10.1016/j.surfin.2025.108097.

38. H. Yan, J. Chen, J. Xia, et al., "In-Situ Engineered Ternary Heterojunction Arrays for High Photoelectric Efficiency Dye-Sensitized Solar Cells," *Solar Energy* 301 (2025): 113956, https://doi.org/10.1016/j.solener.2025.113956.

39. O. Mashtalir, M. R. Lukatskaya, M.-Q. Zhao, M. W. Barsoum, and Y. Gogotsi, "Amine-Assisted Delamination of Nb$_2$C MXene for Li-Ion Energy Storage Devices," *Advanced Materials* 27, no. 23 (2015): 3501–3506, https://doi.org/10.1002/adma.201500604.

40. Z. Lin, L. Liu, and W. Wang, "The Role and Mechanism of Polydopamine and Cuttlefish Ink Melanin Carrying Copper Ion Nanoparticles in Antibacterial Properties and Promoting Wound Healing," *Biomaterials Science* 9, no. 17 (2021): 5951–5964, https://doi.org/10.1039/d1bm00622c.

41. N. Mohamed, "Effect of Some Aluminum Salts-Amine Ionic Liquids on Several Serum Human Parameters and Bacterial Growth of Klebsiella pneumoniae and Staphylococcus aureus," *Journal of Al-Nahrain University-Science* 21, no. 1 (2018): 14–22, https://doi.org/10.22401/JUNS.21.1.03.

42. V. Misha, A. J. McBain, E. Craig, and A. Kathryn, "Single and Combined Antimicrobial Efficacies for Nine Metal Ion Solutions Against Klebsiella Pneumoniae, Acinetobacter Baumannii and Enterococcus Faecium," *International Biodeterioration & Biodegradation* 141 (2019): 39–43, https://doi.org/10.1016/j.ibiod.2018.06.017.

43. O.-S. Lee, M. E. Madjet, and K. A. Mahmoud, "Antibacterial Mechanism of Multifunctional MXene Nanosheets: Domain Formation and Phase Transition in Lipid Bilayer," *Nano Letters* 21, no. 19 (2021): 8510–8517, https://doi.org/10.1021/acs.nanolett.1c01986.

44. Y. Ma, Y. Yue, H. Zhang, et al., "3D Synergistical MXene/Reduced Graphene Oxide Aerogel for a Piezoresistive Sensor," *ACS Nano* 12, no. 4 (2018): 3209–3216, https://doi.org/10.1021/acsnano.7b06909.

45. K. Rasool, M. Helal, A. Ali, C. E. Ren, Y. Gogotsi, and K. A. Mahmoud, "Antibacterial Activity of Ti$_3$C$_2$T$_x$ MXene," *ACS Nano* 10, no. 3 (2016): 3674–3684, https://doi.org/10.1021/acsnano.6b00181.

46. K. Abe, N. Nomura, and S. Suzuki, "Biofilms: Hot Spots of Horizontal Gene Transfer (HGT) in Aquatic Environments, With a Focus on a New HGT Mechanism," *FEMS Microbiology Ecology* 96, no. 5 (2020): fiaa031, https://doi.org/10.1093/femsec/fiaa031.

47. Y. Sang, W. Li, and H. Liu, "Construction of Nanozyme-Hydrogel for Enhanced Capture and Elimination of Bacteria," *Advanced Functional Materials* 29, no. 22 (2019): 1900518, https://doi.org/10.1002/adfm.201900518.

48. D. Rebleanu, C. Gaidau, G. Voicu, et al., "The Impact of Photocatalytic Ag/TiO$_2$ and Ag/N-TiO$_2$ Nanoparticles on Human Keratinocytes and Epithelial Lung Cells," *Toxicology* 416 (2019): 30–43, https://doi.org/10.1016/j.tox.2019.01.013.

49. X. Huang, J. Wang, H. Wang, et al., "Silver–Catechol Dynamic Redox Chemistry Provides Hydrogel Dressings With Sustained Antioxidant and Antibacterial Activity for Chronic Wound Care," *ACS Nano* 19, no. 24 (2025): 22270–22290, https://doi.org/10.1021/acsnano.5c04690.

50. J. Huang, J. Su, Z. Hou, et al., "Cytocompatibility of Ti$_3$C$_2$T$_x$ MXene With Red Blood Cells and Human Umbilical Vein Endothelial Cells and the Underlying Mechanisms," *Chemical Research in Toxicology* 36, no. 3 (2023): 347–359, https://doi.org/10.1021/acs.chemrestox.2c00154.

51. D. Patil, M. Overland, M. Stoller, and K. Chatterjee, "Bioinspired Nanostructured Bactericidal Surfaces," *Current Opinion in Chemical Engineering* 34 (2021): 100741, https://doi.org/10.1016/j.coche.2021.100741.

52. A. Roya and K. Chatterjee, "Theoretical and Computational Investigations Into Mechanobactericidal Activity of Nanostructures at the Bacteria-Biomaterial Interface: A Critical Review," *Nanoscale* 13 (2021): 647–658, https://doi.org/10.1039/D0NR07976F.

53. G. Norman, C. Shi, M. Westby, et al., "Bacteria and Bioburden and Healing in Complex Wounds: A Prognostic Systematic Review," *Wound Repair and Regeneration* 29, no. 3 (2021): 466–477, https://doi.org/10.1111/wrr.12898.

54. G. Mao, W. Yi, Y. Yang, et al., "Novel Antibiotic-Derived Silicon Dots With Broad-Spectrum Antibacterial Activity and Efficient Wound Healing Promotion," *Small* 22, no. 10 (2026): 12500, https://doi.org/10.1002/smll.202512500.

55. S. Wang, Y. Zhao, A. P. Breslawec, et al., “Strategy to Combat Biofilms: A Focus on Biofilm Dispersal Enzymes, Npj Biofilms and Microbiomes,” *npj Biofilms and Microbiomes* 9, no. 1 (2023): 63, https://doi.org/10.1038/s41522-023-00427-y.

56. X. Shi, Z. Yu, Z. Liu, et al., “Scalable, High-Yield Monolayer MXene Preparation From Multilayer MXene for Many Applications,” *Angewandte Chemie International Edition* 64, no. 6 (2025): 202418420, https://doi.org/10.1002/anie.

57. X. Zhu, Y. Zhu, K. Jia, et al., “A Near-Infrared Light-Mediated Antimicrobial Based on Ag/$Ti_3C_2T_x$ for Effective Synergetic Antibacterial Applications,” *Nanoscale* 12, no. 37 (2020): 19129–19141, https://doi.org/10.1039/d0nr04925e.

58. R. Zhang, W. Li, Z. Guo, et al., “Valence Electron Fluctuation in a High-Entropy Oxide Heterojunction Enables Collaborative Photodynamic and Mild-Thermal Therapy for Cutaneous Biofilm Infections,” *ACS Nano* 19, no. 23 (2025): 21348–21364, https://doi.org/10.1021/acsnano.4c18444.

Supporting Information

Additional supporting information can be found online in the Supporting Information section.

Supporting File: smll73934-sup-0001-SuppMat.docx.